

Performance Evaluation for Retrieving Aerosol Optical Depth from Directional Polarimetric Camera (DPC) based on GRASP Algorithm

Shikuan Jin¹, Yingying Ma^{1,2,*}, Cheng Chen^{4,5}, Oleg Dubovik⁵, Jin Hong⁶, Boming Liu¹, Wei Gong^{2,3}

¹ State Key Laboratory of Information Engineering in Surveying, Mapping and Remote Sensing, Wuhan University, China.

² Collaborative Innovation Center for Geospatial Technology, Wuhan 430079, China.

³ School of Electronic Information, Wuhan University, China.

⁴ GRASP-SAS, Remote Sensing Developments, Cite Scientifique, 59655 Villeneuve d'Ascq, France.

⁵ Univ. Lille, CNRS, UMR 8518 - LOA - Laboratoire d'Optique Atmosphérique, Lille, France.

⁶ Anhui Institute of Optics and Fine Mechanics, Chinese Academy of Sciences, Hefei 230031, China.

Corresponding Author: Yingying Ma (yym863@whu.edu.cn)

Abstract

Aerosol spatial distribution obtained from satellite sensors is critical for understanding regional aerosol environments, anthropogenic aerosol emissions, and global climate change. Directional Polarimetric Camera (DPC) is the first generation of multi-angle polarized sensor developed by China. It is onboard GaoFen-5 satellite, running in 705 km sun-synchronous orbit with a 13:30 pm ascending node. The sensor has three polarized channels at 490, 670, and 865 nm and ~9 viewing angles, mainly used for observing aerosols. The spatial resolution is ~ 3.3 km at nadir and global coverage is ~2 days. In this study, the performance of aerosol optical depth (AOD) retrievals from the DPC/GaoFen-5 using the Generalized Retrieval of Atmosphere and Surface Properties (GRASP) algorithm were evaluated on a global basis for the first time. The results showed that the DPC GRASP/Models scheme, which used several aerosol-type mixings, achieved good performance. By comparing with AERONET observations, the correlation coefficient (R), root mean square error, and Expected Error (EE%, $\pm(0.05+0.15*AOD)$) were 0.9007, 0.0662, and 82.54%, respectively. The scattering angle, number of averaged pixels, length of timesteps, and radiative and polarized fitting residuals showed impacts on the results of AOD retrieval in the DPC GRASP/Models. From the most of AERONET sites, the R and EE% were larger than ~0.9 and ~80%. Compared with MODIS products, the spatial and temporal variations of aerosol could be caught by the DPC with the GRASP/Models, showing a good performance. However, values of AOD were also underestimated by DPC, probably due to overstrict cloud mask. The above findings validated the ability of the DPC sensor to monitor aerosols. It should contribute to the development of aerosol parameter retrieval from multi-angular polarized sensors in the future.

Key Words: GRASP/Models, Aerosol Optical Depth, Directional Polarimetric Camera, GaoFen-5,

42 **1. Introduction**

43 Aerosol is one of the most important components in the atmosphere. They influence the global
44 radiation budget balance and climate directly by scattering and absorbing incoming solar radiation
45 and indirectly by changing cloud microphysical properties (Albrecht 1989; Rosenfeld et al. 2008).
46 Due to the different emission sources and relatively transitory lifecycle in the atmosphere, aerosol
47 particles show large spatiotemporal variability, and are difficult to describe uniformly at a global
48 scale (Eck et al. 2010; Jin et al. 2019; Ma et al. 2021). This property can further affect atmospheric
49 motions, the hydrological cycle, and probably contribute to regional extreme weather events (Guo
50 et al. 2016; Li et al. 2016; Nakajima et al. 2007; Shi et al. 2021). Therefore, the development of
51 aerosol measurement technologies has received widespread attention in recent decades.

52 Satellite observation is the main approach to monitor and quantify aerosol distributions at a
53 global scale (Kaufman et al. 1997). Traditional satellite technology relies on prior assumptions about
54 the properties of the surface and atmosphere, because the prerequisite for successful retrieval of
55 aerosol is that the aerosol signal should be isolated from the remainder of the signal received by
56 satellite, which includes the combined effect from molecule, aerosol, cloud, and the underlying
57 surface (Lenoble et al. 2013). For instance, the appropriate spatial resolution helps to observe
58 aerosol through clear holes in otherwise cloudy skies (Jin et al. 2021). The choice of spectral channel
59 and bandwidth can avoid impact by gas absorption in narrow spectral bands known as atmosphere
60 window regions. More importantly, the spectral channel should be set in a carefully selected band
61 to avoid introducing uncertainty from underlying surface features, such as vegetation, bright desert,
62 and ocean color (Hsu et al. 2004; McCormick et al. 1979; Rao et al. 1989). Based on these principles,
63 a series of aerosol products from different sensors have been released, and they greatly promote the
64 developments of studies in aerosol-related fields, including aerosol climate effect, interaction of
65 aerosol and cloud, air quality and public health, and global climate modeling (Gao et al. 2017; Liu
66 et al. 2022; Sayer et al. 2013; Tegen and Lacis 1996; Zhang et al. 2021).

67 With the progress of satellite technology, sensors with broader spectral range, multiple angles,
68 and polarization observations have been applied to aerosol observations (Dubovik et al. 2019).
69 POLDER-3 is the third sensor in the POLarization and Directionality of the Earth's Reflectance
70 series, carried on the Polarization and Anisotropy of Reflectances for Atmospheric Science coupled
71 with Observations from a Lidar (PARASOL), which was launched on December 18, 2004, as part
72 of the A-Train (Tanre et al. 2011). This instrument views ($\pm 51^\circ$ along track and $\pm 43^\circ$ across track)
73 Earth from ~ 14 different angles by using a set of wide-field telecentric optics and a rotating filter
74 wheel in nine spectral channels from 443 to 1020 nm (Deschamps et al. 1994). Among them, three
75 channels at 490, 670, and 865 nm have polarization observation capabilities. POLDER-3 provides
76 the longest multi-angle polarimetric observation record of the Earth-atmosphere system in space to
77 date and the PARASOL mission was terminated in December 2013 due to limited on-board fuel.
78 The Directional Polarimetric Camera (DPC) is the first Chinese multi-angle polarized Earth
79 observation satellite sensor, onboard the fifth satellite (GaoFen-5) of the Chinese High-resolution
80 Earth Observation Program (Li et al. 2018). It was launched successfully on May 9, 2018, with the
81 purposes of measuring aerosol parameters and providing information for the assessment of urban
82 air pollution. The design of DPC is similar to the POLDER-3. It is equipped with five non-polarized

83 bands at 443, 565, 763,765, and 910 nm and three polarized bands at 490, 670, and 865 nm, with [a](#)
84 relatively ~~high~~[high](#) spatial resolution of 3.3 km, that can observe Earth from ~9 different angles.
85 Therefore, the DPC occupies an important position in the development of polarization instruments
86 in China, and is expected to provide beneficial information for atmospheric aerosol monitoring and
87 satellite payload research.

88 The multi-angular polarized sensor can provide many more observations for the same pixel in
89 an aerosol parameter ~~retrieval~~[retrieval](#). Compared to traditional spectral measurement, the multi-
90 angle can help constrain bidirectional reflections function, reducing uncertainty from the surface
91 (Diner et al. 1998), while the polarized signal is mainly from atmospheric aerosol and sensitive to
92 particle microphysical properties (Mishchenko and Travis 1997). Generally, the polarized signal can
93 be considered as an independent source of information. A well-known advantage is that the polarized
94 light from the surface ~~is~~ accounts for a small part of the total polarized light compared with that
95 from the particles and is mostly wavelength independent. In the algorithms for POLDER, the
96 polarized signals at 670 and 865 nm are used for deriving the best aerosol model over the ocean and
97 retrieving Aerosol Optical Depth (AOD) over land, due to the sensitivity to fine particles (Deuzé et
98 al. 2001; Ge et al. 2020; Kacenelenbogen et al. 2006; Nadal and Bréon 1999). In addition, the
99 existence of the cloudbow effect in the polarized signal can also be used to recognize cloud mask
100 and detect cloud structure (Breon and Colzy 1999; Breon and Goloub 1998; Li et al. 2021).

101 However, the algorithms that retrieve aerosol parameters from only one or two polarized
102 channels struggle to obtain complex aerosol optical and microphysical parameters, such as aerosol
103 size distribution and absorbing and scattering properties. To solve this problem, the Generalized
104 Retrieval of Atmosphere and Surface Properties (GRASP) algorithm was developed, which provides
105 a statistical optimized strategy that allows all aerosol-related measurement data from multi-angular
106 polarized sensors to participate in the retrieval (Dubovik et al. 2014). It points out that the measured
107 redundancy provided by multi-angular polarized sensor is considered to be positive and useful,
108 especially when the number of observations is larger than the unknowns (Dubovik et al. 2011). At
109 present, the GRASP algorithm has been successfully applied to a variety of sensors, including
110 POLDER, lidar, and sun photometer, to retrieve complex aerosol parameters (Chen et al. 2020; Li
111 et al. 2019; Lopatin et al. 2021). In this study, we retrieved AOD from DPC observations by using
112 GRASP algorithm and evaluated possible error influencing factors. At the same time, by comparing
113 MODIS and AERONET observations, the aerosol monitoring performance of DPC were verified in
114 different space and time scales. This will partially lay the foundation for the retrieval of aerosol
115 parameters from multi-angular polarized sensors in the future of China.

116 2. Satellite and Ground-based Data

117 2.1 DPC Data

118 The DPC is a multi-angular polarized sensor carried on the GF-5 satellite, which was launched
119 in May 9, 2018. This sensor completes a scan of entire Earth's surface about every two days from a
120 sun-synchronous orbit and provides a swath of 1850 km with a spatial resolution of 3.3 km (Li et
121 al. 2018). The DPC contains eight bands from 443 to 910 nm with a bandwidth of 10-40 nm that
122 can observe ~~earth~~[Earth](#) from ~9 different angles in a local time of ~13:30 PM. Along with channels
123 for water vapor (910 nm) and pressure (Oxygen A band: 763 and 765 nm), five bands (443, 490,

124 565, 670, and 865 nm) are designed to measure aerosols (Li et al. 2018). The polarimetric capability
125 at 490, 670, and 865 nm is realized by a polarized filter wheel (0° , 60° , and 120°) and a step motor
126 (Hagolle et al. 1999). The laboratory calibration uncertainties are 5% for normalized radiation and
127 0.02 for Degree Of Linear Polarization (DOLP) (Li et al. 2021). An in-flight calibration study
128 showed that the radiometric calibration error increased to $\sim 9\%$ at 865 nm and the polarimetric
129 calibration error increases to ~ 0.04 at 490 and 670 nm after launch, by respectively applying
130 Rayleigh and glint scenes over ocean (Qie et al. 2021). Degradation of instrument performance over
131 time may result in higher negative radiometric shift (Zhu et al. 2022). Thus, additional correction
132 coefficients were also applied in this study to correct the image of the DPC observations from March
133 to April, 2020. The processing of DPC data is described in Section 3.2 in detail.

134 2.2 MODIS aerosol products

135 The Moderate-resolution Imaging Spectroradiometer (MODIS) has been in service for over
136 two decades, providing valuable Earth's observations. The MODIS Level 2 C6.1 aerosol product
137 (MxD04) is generated by using Dark Target (DT) algorithm and Deep Blue (DB) algorithm (Hsu et
138 al. 2013; Levy et al. 2013). It provides multi-wavelength AOD data from each individual image
139 with spatial resolutions of 3 km and 10 km. The MODIS Level 2 C6 aerosol product (MCD19A2)
140 calculates aerosol parameters by using the Multi-Angle Implementation of Atmospheric Correction
141 (MAIAC) algorithm from the continuous scenes of two satellites (Terra and Aqua) and considers
142 temporal and spatial correlation of aerosols, with spatial resolution of 1 km (Lyapustin et al. 2018).
143 DT algorithm provides retrievals over ocean and land except for bright surfaces (such as desert dust),
144 while the DB algorithm is only applied over land, and the MAIAC algorithm is used over land and
145 part of the surrounding ocean. These MODIS aerosol products have been rigorously tested and
146 verified, and are widely used in aerosol-related studies (Che et al. 2019; Sayer et al. 2014; Zhdanova
147 et al. 2020). In this study, the corrected AOD (quality flag = 3) on land and average AOD (quality
148 flag = 1,2,3) on the ocean are selected from the DT products. The best estimated AOD (quality flag
149 = 2,3) is selected in the DB products. The best quality AOD (QA AOD = 0000) is selected in the
150 MAIAC products.

151 2.3 AERONET observations

152 The AERosol RObotic NETwork (AERONET) is a federation of ground-based remote sensing
153 aerosol networks, established and expanded by various institutions from different countries (Holben
154 et al. 1998). It has contributed continuous and long-term aerosol optical, microphysical, and
155 radiative properties for more than 25 years in major ecosystems and human activity areas around
156 the world. The AOD data used for validation were acquired from 178 AERONET sites with Level
157 2.0 AOD products, which have been cloud-screened and quality controlled. The uncertainties of
158 AOD are less than 0.02 (Eck et al. 1999). In order to match the AERONET data to the satellite
159 observations, a common approach is followed to average satellite data within ± 30 min and a circle
160 of 0.25° (~ 25 km) radius centered at the selected site (Sayer et al. 2013). The relationship between
161 multi-wavelength AOD proposed by Ångström (1964) was applied to calculate the AOD at
162 corresponding wavelength of satellite bands from AERONET data.

163 3. Methods

164 3.1 Introduction of GRASP algorithm

165 GRASP is an open-source software package (<https://www.grasp-open.com/>) for calculating
166 and retrieving various optical and microphysical properties of aerosol and surface from observations
167 of different remote sensing instruments, such as satellite, lidar, radiometer, and radiosonde (Dubovik
168 et al. 2021). It was originally designed to solve the problem of aerosol retrieval from the PARASOL
169 observations (Dubovik et al. 2014), while now has become a scientifically rigorous and versatile
170 algorithm based on generalization principles that works with diverse remote sensing applications in
171 the community after continuous development (Dubovik et al. 2021). The GRASP algorithm contains
172 two pivotal and independent modules. One is used to calculate the scattering, absorption, and
173 extinction of light between different media from the physical level, simulating theoretical
174 observational radiation signal, called “Forward Model”. It allows definition of various complex
175 aerosol (size distribution, refractive index, and sphere fraction, etc.) and surface properties
176 (Bidirectional Reflectance/-Polarization Distribution Function, BR/PDF, etc.) in the construction of
177 the modelled reflectance. Therefore, it is possible to transform from optical observations to aerosol
178 microphysical properties and estimate the surface parameters (Dubovik et al. 2011). The other
179 module can be thought of as general mathematical operations without any particularly physical
180 nature, called “Numerical Inversion”. It follows the statistically optimized strategy to fit
181 observations under the fundamental frameworks of the Maximum Likelihood Method and multi-
182 term Least Square Method (Dubovik and King 2000). GRASP also realizes multiple-pixel retrieval,
183 which constrains the variability of aerosol and surface optical properties in fitting process by an
184 extra prior knowledge. Due to the consideration of the surrounding pixel information, the multi-
185 pixel retrieval is more stable, and more importantly, it can make up for the lack of aerosol reflection
186 information in some cases, such as conditions that the signal from aerosol is much less than that
187 from the surface (Dubovik et al. 2011). Based on the above advantages, the GRASP supports input
188 measurements/parameters from different sources and levels, such as normalized and polarized
189 radiance, vertical extinction and backscatter profile, and optical depth. This avoids that the most
190 popular look-up table-based methods are difficult to apply to each other, due to the limitations of
191 different sensor channel and characteristic.

192 3.2 Pre-processing of DPC Data

193 In order to partially offset the signal attenuation due to instrument aging, before the pre-
194 processing and retrieval, the radiance signals from the DPC were transferred and corrected to
195 normalized radiative and polarized reflectance at top of the atmosphere, as equation 1.

$$196 [I_N, Q_N, U_N]^T = \pi \cdot [I, Q, U]^T / [E_0 \cdot A'_k(\theta_0) \cdot P'_k(\theta)] \quad (1)$$

197 where, the $[I, Q, U]^T$ are represent the radiative and polarized radiances, received by the DPC, in
198 the form of the first three parts of the Stokes vector. The $A'_k(\theta_0)$ and $P'_k(\theta)$ are the two additional
199 correction coefficients. For I , they are applied following the results of Zhu et al. (2022), which
200 depends on the view zenith angle (θ) and calculated based on Rayleigh scenes over sea surface. For
201 polarimetric signals, the additional correction coefficients can be referred to Qie et al. (2021). The
202 E_0 is the standard solar radiation flux and the $[I_N, Q_N, U_N]^T$ are the corrected normalized signals
203 at top of the atmosphere of DPC.

204 In successful AOD retrieval, one of the key processes is to screen appropriate pixels. Cloudy
205 pixels ~~is~~ are the main factor impacting aerosol retrieval, because they will block the signal from
206 aerosol due to high reflectance, large coverage, and relatively high vertical position. Even very thin
207 cirrus clouds and missed cloud edges can cause an positive error of ~13% in visible channel (Koren
208 et al. 2007). To remove cloud pixels in DPC images, we used several universal methods by
209 considering cloud-sensitive characteristics in radiative and polarized bands:

210 1) The first step is to filter the image with a 3×3 sliding window at the blue (490 nm) and red
211 (670 nm) bands for land and sea surfaces, respectively (Remer et al. 2012). If the standard deviation
212 of a window is greater than 0.0025, then the center pixel will be marked as a cloud pixel and removed
213 (Martins et al. 2002). This method was initially applied to the MODIS image by considering the
214 spatial variability of aerosol and cloud pixels. In addition, a threshold of > 0.4 in the green (565 nm)
215 band is also used to detect cloud pixels after the filter process, in accordance with the DT algorithm.
216 This threshold is to exclude very uniformly distributed cloud pixels in the central area of thick clouds,
217 and some snow pixels and glint area will also be excluded at the same time.

218 2) In second step, a whiteness test was applied by using reflectance in visible bands. It uses the
219 characteristic that clouds are white in the visible band, considering that pixel with the absolute value
220 of relative deviations greater than 0.7 is cloud, as equation 2-3.

$$221 \quad \text{MeanVis} = (\text{Band}_1 + \text{Band}_2 + \text{Band}_3)/3 \quad (2)$$

$$222 \quad \text{Whiteness Test} = \sum_{i=1}^3 |(\text{Band}_i - \text{MeanVis})/\text{MeanVis}| > 0.7 \quad (3)$$

223 Where, Band_1 , Band_2 , and Band_3 are reflectance in red, green, and blue bands received by
224 satellite at top of the atmosphere, respectively. Corresponding to the DPC, they are 490, 565, and
225 670 nm, respectively. In the absence of infrared and thermal infrared information, it can
226 supplementally remove any pixels that have flat reflectance, similar to some operators using
227 reflectance ratio to detect clouds. This method was proposed by Gomez-Chova et al. (2007) for
228 Medium Resolution Imaging Spectrometer (MERIS) multispectral image, and it has also been
229 considered in the well-known Fmask algorithm (Zhu and Woodcock 2012).

230 3) The third step used polarized bands to remove cloud pixels, following a fact that cloud drops
231 can show a relatively strong polarized reflectance by multiple scattering (cloudbow effect) under a
232 specify observation geometry. This feature has been used to a generate cloud mask product for both
233 POLDER and DPC sensors (Breon and Colzy 1999; Li et al. 2021). When the scattering angle (SCA)
234 is between 127° and 157°, pixels with corrected polarized radiation at 865 nm larger than 0.03 and
235 0.05 for ocean and surface, respectively, are defined as cloud (Li et al. 2021). The relatively large
236 SCA range is for a strict screening, given that the main peak of the polarized reflectance by cloud
237 water droplets is ~142° (Goloub and Deuze 1994). In addition, any obvious noise is also removed
238 in this step, such as the case of DOLP > 1.

239 3.3 Construction of Multi-pixel Retrieval Unit

240 Next, we will explain the necessary operations and settings of parameters to apply the GRASP
241 algorithm to DPC data in detail. The GRASP algorithm can use the temporal and spatial continuity
242 of pixels, and allow a group of pixels to be inverted at the same time. The multi-pixel retrieval unit
243 for DPC in the study is shown as **Figure 1**. Each small cube represents a pixel in geographic grids
244 with a spatial resolution of 0.1°×0.1° (3×3 DPC pixel averaged). This is in accordance with the
245 MODIS 04_L2 product (~10 km). The projection is determined by the DPC data. Each pixel is
246 guaranteed to have at least 3 different observation angles. Size of the retrieval unit can be arbitrarily

247 selected, but is limited by the hardware memory. Different colors show the percentage of land or
248 sea, and usually do not change with time. They need to be clearly defined in GRASP to select
249 different surface reflectance models. Cloud and no-data pixels need to be removed before the
250 retrieval, because the cloud flag setting has not been implemented in the current version of code.
251 Finally, this retrieval unit was processed using the GRASP algorithm to derive the AOD
252 distributions.

253 3.4 Settings of Retrieval Parameters

254 The settings of initial value and spatial-temporal constraint can significantly impact results of
255 the statistically optimized strategy in the GRASP algorithm (Dubovik et al. 2011). The GRASP
256 allows several strategies to fit observations. For instances, the GRASP software gives two retrieval
257 schemes for POLDER observations. The configurations of the two schemes are different only by
258 settings of aerosol size distribution in the forward model. One fits the aerosol size distribution with
259 16 triangle bins from the range of 0.05 to 15.0 μm , while the other uses 5 lognormal bins at 0.1,
260 0.1732, 0.3, 1.0, and 2.9 μm , based on pre-calculated optimized kernels of the POLDER-3. The 5
261 lognormal bins scheme increases speed by ~ 9 times (2.5GHz CPU) without any
262 graphical acceleration compared to the 16 triangle bins scheme, and it has been used to generate the
263 operational PARASOL/GRASP aerosol products (Chen et al. 2020). In addition, there is a scheme
264 that is being tested called “GRASP/Models”. The GRASP/Models approach assumes ~~by-an~~
265 ~~externally~~ mixing-mixture of several aerosol types with fixed optical parameters, which is fast and
266 more stable AOD retrieval especially when aerosol loading is low (Chen et al., 2020).

267 A tolerable absolute error in radiative transfer calculations is set to 0.0005 and the multiple
268 scattering effects have been considered. The number of atmospheric layers is set to 10 with an
269 exponential distribution. The input data of the GRASP algorithm was both normalized radiative
270 measurements at 443, 490, 565, and 670 nm and DOLP of 490 and 670 nm. The initial guess of
271 aerosol and surface properties are default in the GRASP software. They are applied to calculate
272 AOD at a global scale. The Ross-Li’s model (Li and Strahler 1992) and the Cox-Munk model (Cox
273 and Munk 1954) were used for modeling radiative (non-polarized) reflectance over land and ocean,
274 respectively, while, the surface polarized reflectance followed the method of Nadal and Bréon
275 (1999). More details are documented in Dubovik et al. (2011). Among them, the complex refractive
276 index and surface properties are generally allowed to be fit as wavelength-dependent parameters in
277 iterations. All constraints on values are given a default sizeable range, such as the first parameter in
278 the Ross-Li’s model allowed to vary from 0.001 to 1.100. By light scattering calculations (Dubovik
279 et al. 2006), all aerosol microphysical parameters are converted into optical parameters to participate
280 in radiative simulation. Spatial and temporal constraints of variabilities of aerosol and surface
281 properties are realized ~~by~~-using Lagrange multiplier method. More details can be referred to
282 Dubovik et al. (2021). In this study, the GRASP/Models scheme was used to retrieve AOD from
283 DPC. All calculations of the GRASP relied on the supercomputing system in the Supercomputing
284 Center of Wuhan University.

285 4. Results and Discussions

286 4.1 Validation of DPC/GRASP with AERONET

287 As shown in **Figure 2**, the AERONET observations were used as the references to estimate the
288 performance of AOD retrieval from DPC images based on the GRASP algorithm. Linear regression,
289 correlation coefficient (R), Root Mean Square Error (RMSE), Mean Bias (MB), percentage falling
290 into Expected Error (EE%, $\pm(0.05+0.15*AOD)$), and matching Number (N) were also calculated.
291 Among them, the EE% is selected in accordance with the MODIS error envelop and the ideal EE%
292 is ~68% under assumption of normal distribution within one sigma confidence interval. Overall, the
293 DPC GRASP/Models AOD matches the AERONET observations with an R of 0.8511, a MB of
294 0.0256, and a RMSE of 0.0842, showing good performance without any quality control. Nearly 80%
295 of the GRASP/Models AOD retrievals fall within the EE% bounds, revealing that the error envelop
296 of DPC is probably narrower than that of MODIS. While, the slope of linear regression was 0.8686,
297 less than 1. This means that under heavy aerosol loading, the DPC/GRASP probably underestimates
298 the AOD. More details are presented in **Figure 2c**. It is found the lower slope of linear regression is
299 mainly controlled by several points which have larger AOD (> 0.8). By contrast, when AOD is less
300 than 0.8, the retrieval is stable.

301 In order to further study the retrieval performance of GRASP/Models and control the quality
302 of the retrieval result from DPC data, we calculated the dependences of absolute MB with retrieval
303 residuals, timesteps (serial length) and average pixel (involved in retrieval) number in retrieval units,
304 and observation geometry, as shown in **Figure 3**. The retrieval absolute MB showed an obvious
305 increase when the SCA is larger than 150° . Critical observation conditions, such as pixels at the
306 edge of the image, will probably result to a larger error in both satellite sensor and forward model.
307 By contrast, different viewing angle number (3-11) have relatively little impact on the retrieval
308 results, with the absolute MB per bin ranging between 0.0296 and 0.0595. With increase in timesteps,
309 the absolute MB showed a slightly decreasing trend, from 0.0543 to 0.0561. The same phenomenon
310 was also found in the **Figure 3d**. The absolute MB decreased from 0.0691 to 0.0435 with the number
311 of averaged pixels increasing. This indicated that the fitting scheme for using the external mixing
312 of different aerosol types in this scheme of the GRASP/Models showed positive dependence of the
313 length of timesteps and number of pixels. In addition, the spatial-temporal constraints in the retrieval
314 are also affected by Lagrange multipliers, which can be customized in the configuration file.

315 Fitting residual is an important factor to estimate the quality of retrieval in GRASP. It was
316 found that the absolute MB showed a slight increase (from 0.0397 to 0.0596) when the radiative
317 fitting residuals were larger than 8%. While, the absolute MB had a trend to decrease first and then
318 increase, with increase in the polarized fitting residuals. Given that the DPC designed uncertainty
319 is about 5% for radiometric measurements and 0.02 for DOLP, the relatively large absolute MB
320 (0.069) at 0.01 of the polarized fitting residuals is probably caused by the noise. To summarize, the
321 SCA, number of averaged pixels, and fitting residuals showed the impacts on DPC GRASP/Models
322 AOD retrieval in this test. Retrieval is considered low quality if any of the following conditions are
323 met: 1) Pixels with SCA > 150 ; 2) number of averaged pixels < 4 ; 3) length of timesteps < 5 ; 4)
324 non-polarized fitting residual $> 8\%$; 5) polarized fitting residual > 0.06 .

325 **Figure 4a-b** shows the scatterplots and density distributions of DPC/GRASP AOD versus the
326 AERONET observations after quality control. About 20% of the points were removed. It was found
327 that the performance of AOD retrieval from DPC images showed an enhancement. For DPC
328 GRASP/Models, the R increased from 0.8511 to 0.9001, the EE% increased from 79.30% to 82.54%,
329 the RMSE decreased from 0.0842 to 0.0662, and the MB decreased from 0.0256 to 0.0234. **Figure**
330 **4c** ~~displayed~~ displays the changes of differences between DPC and AEROENT AOD. The

331 underestimations when $AOD > 0.8$ were not found to be restrained by the quality control. A possible
332 reason is that an overly restrictive cloud mask can remove aerosol pixels during heavy pollution. In
333 addition, the negative drift after the launch of the DPC may also be the reason, if it is not fully
334 corrected.

335 4.2 Evaluation of DPC AOD Performance at a Spatial Scale

336 The DPC AOD retrieved by the GRASP/Models were compared with AERONET observations
337 at each individual site to show a world-wide retrieval result as **Figure 5**. The R, RMSE, MB, and
338 EE% were calculated and displayed for sites where the matching number of pixels was larger than
339 5. In addition to the observation performance of the DPC itself, spatial variations in performances
340 of AOD retrieval greatly depend on settings of initial parameter and constraint in the GRASP,
341 whether they are in line with the local aerosol and surface environments. Results showed that the
342 GRASP/Models achieved a great performance in different regions. The high values of R (> 0.8)
343 were found in most regions, while the ~~several~~ lower values (~ 0.6) were mainly observed in North
344 America. The values of RMSE at most sites were less than 0.08. These suggest that most values of
345 AOD retrieval matched the AERONET AOD very well. At several sites, such as Asia and Africa,
346 the RMSE were larger than 0.2, revealing that the AOD has a relatively larger deviation calculated
347 from DPC images based on current parameter setting with the GRASP algorithm in the regions.
348 From the MB of **Figure 5c**, the values of AOD were overestimated (~ 0.04) in ~~the~~ most areas. By
349 contrast, the underestimations were found in high aerosol loading regions, such as South Asia and
350 North Africa, that MB values were between -0.02 and -0.10, in accordance with the large
351 underestimation when $AOD > 0.8$ mentioned above. The EE% showed that over 80% of AOD
352 retrieved in sites can fall within the expected error range. It is worth noting that the parameterization
353 in the GRASP/Models scheme is a globally consistent configuration in this study and does not
354 consider the characteristics between different regions. This means that it is possible to achieve better
355 results in local regions by adjusting different parameterizations.

356 To further estimate the performance of DPC/GRASP AOD, two regions were selected as cases
357 as shown in **Figure 6**. The MODIS MAIAC, DT, and DB aerosol products were used as comparisons.
358 It was noted that the DB algorithm was only executed over land in the C6.1 MODIS DB aerosol
359 products. It was found that the spatial coverage of GRASP/Models AOD from DPC over land was
360 slightly lower than the MAIAC MODIS aerosol products. In addition to the narrower field of view
361 and longer re-visit cycle on DPC (MODIS operated in two satellite: Terra and Aqua), the cloud mask
362 method probably also mis-classified the cloud-free pixels in heavy aerosol loading conditions. This
363 also partially resulted in the underestimation of DPC AOD because the heavy aerosol loading pixels
364 are removed. Nevertheless, DPC still properly captures the spatial distribution of AOD. The highest
365 AOD values (> 1.0) in the southern part of China (mainly Guangdong and Guangxi) were caught
366 by the current retrieval strategy. This is in accordance with the three MODIS products. By contrast,
367 the AOD found in North China Plain and Centre China by the DPC GRASP/Models (~ 0.5) were a
368 little bit lower than MAIAC and DT products (~ 0.6). However, the DT aerosol products showed
369 higher AOD in this region, closed to ~ 1.0 . This phenomenon is caused by unsuitable aerosol models,
370 which further results in a persistent overestimation in the DT algorithm~~This phenomenon owes to~~
371 ~~unsuitable aerosol models, which further results a persistent overestimation in DT algorithm~~ (Che
372 et al. 2019). By the additional radiometric and polarimetric correction, the DPC GRASP/Models
373 showed good performance over both Land and Ocean. The high values of AOD in the South China

374 Sea and the estuary of the Yangtze River can be clearly captured. To summarize, the DPC showed
375 spatial ability of AOD retrieval based on GRASP algorithm in China region and the similar results
376 have also been reported recently by using the GRASP/component module (Li et al. 2022).

377 Another case was selected in Western Europe where the air is clean and aerosol loading is low
378 (< 0.2) ~~in the most of time around year~~most of the year. As shown in **Figure 6b**, different satellites
379 and aerosol retrieval methods showed slightly different distributions of AOD. In addition to the
380 different transit times between DPC and MODIS, this phenomenon is also probably because the
381 aerosol signal is difficult to separate from the remainder of signal under low aerosol loading
382 conditions and thus result in relative larger uncertainties of retrieval. From the AOD maps of DPC
383 GRASP/Models, the relatively high values of AOD (~ 0.25) were found in Central France, Southern
384 Spain, and Southern England. While, the MODIS MAIAC showed lower AOD (~ 0.1) over the
385 mainland and two points of high AOD (~ 0.5) were found in Northern coastal areas of Spain and
386 Algeria. By contrast, the distributions of AOD calculated by DT and DB algorithm were also
387 different from that calculated by DPC GRASP/Models and MAIAC. The high AOD (~ 0.4) region
388 appeared in Northern France, Italy, and Southern England. Compared with single pixel-based
389 retrieval algorithm (such as DT and DB), the GRASP and MAIAC considered more temporal and
390 spatial information of aerosol and surface parameters. And benefit from the consistency of all
391 assumptions (regarding aerosol and a priori constrains), the DPC GRASP exhibits minimal land-sea
392 contrast. All of them have been proven to have good performance of AOD retrieval (Chen et al.
393 2020; Lyapustin et al. 2018; Ou et al. 2021; Sayer et al. 2014).

394 **Figure 7** ~~showed~~shows density distributions of difference between DPC and MODIS products
395 in ranges of $AOD \leq 0.2$, $0.2 < AOD \leq 0.7$, and $AOD > 0.7$. Corresponding to the **Figure 6**, this
396 is used to complement quantitative evaluations for the two regions. ~~It can be found a~~A common
397 pattern ~~showed~~is seen in all sub-plots, namely that the differences were nearly normally distributed,
398 centered on the 0 under low aerosol loading conditions ($AOD \leq 0.2$). With increasing AOD
399 ($AOD > 0.7$), the differences showed an increasing negative bias, with the peak value varying from
400 -0.5 to -1.0 . The DPC GRASP/Models underestimated AOD under heavy aerosol loading conditions,
401 similar to the comparisons with AERONET. In follow-up studies, a more detailed investigation of
402 this problem is required.

403 4.3 Comparison of DPC AOD with MODIS Products at a Temporal Scale

404 In this section, time-series of AOD were evaluated against MODIS aerosol products based on
405 the observations of AERONET site. The time-series of daily RMSE is calculated for the global
406 AERONET data set, as shown in **Figure 8**. Lower value of RMSE means the smaller actual errors,
407 indicating a good match with the AERONET. The AERONET stations had relatively continuous
408 observations during the study ~~period to avoid how global validation statistics shift with the spatial~~
409 ~~distribution of observations~~period to avoid that global validation statistics shift in local emphasis
410 ~~and introduce temporal variation in the global results~~ (Gupta et al. 2018). From the **Figure 8**, it was
411 found that the time series of AOD from DPC GRASP/Models had a good matching with the
412 AERONET AOD. The values of RMSE were ~ 0.06 and stable before 87th day. While the reason of
413 relatively large RMSE (~ 0.12) around 90th day is presumed to be heavy aerosol loading conditions,
414 as the DPC GRASP/Models would underestimate AOD under this situation. The similar temporary
415 rapid increases in RMSE were also found in MODIS products, such as the 80th day of the DT, the
416 85th day of the DB, and 98th day of the MAIAC. This reflects the time instability of algorithms. In

417 addition, the lowest daily averaged RMSE was found in DPC GRASP/Models with value of 0.0663,
418 and then MODIS DT (0.0863) and MODIS DB (0.0913). The low RMSE of DPC may be due to it
419 ignoring some high value AODs. It is worth noting that the same parameter scheme (including start
420 points and constraints) was applied globally in the GRASP/Models. Therefore, the difference in
421 aerosol optical properties and spatial-temporal heterogeneity in different regions may be not
422 considered appropriately. The optimization of the region is expected to improve the retrieval effect
423 and further evaluation also requires the use of longer sequences of DPC data in the future.

424 **Figure 9** ~~showed~~ shows three cases at different underlying surface to display the time series of
425 AOD retrieved from DPC GRASP/Models on the basis of AERONET observations. The DT AOD
426 was also compared as a reference, due to its stable performance. It was found that the behavior of
427 AOD from DPC/GRASP and MODIS DT was generally consistent with AERONET at the three
428 sites. From the scatterplots, the values of R were 0.947 and 0.949, 0.943 and 0.959, and 0.967 and
429 0.859 for MODIS DT and DPC GRASP/Models AOD at Raciborz, Magurele_Inoe, and FZJ-
430 JOYCE, respectively. The GRASP/Models AOD retrieved from DPC were slightly higher than the
431 AERONET in the FZJ-JOYCE site and thus it resulted a relatively lower R. Nevertheless, in general,
432 DPC/GRASP has a good ability to capture the temporal variation of aerosols.

433 **Conclusion and Summary**

434 The DPC/GaoFen-5 is the first multi-angular polarized sensor launched by China and thus it
435 has occupied an important position in the development of satellite sensors. In this study, AOD was
436 retrieved from the DPC images by using the GRASP algorithm and compared with AERONET and
437 MODIS observations. The main purpose ~~is~~ was to evaluate the performance of the DPC to monitor
438 global aerosols.

439 On a global basis, a uniform parameterization scheme, which defined the variation ranges and
440 start values of the optical and microphysical properties (realized by aerosol type) of the aerosol, was
441 applied in the “Model” module of GRASP. Validations against AERONET showed that the R and
442 EE% of DPC GRASP/Models were 0.8511 and 79.30%, respectively, in the first attempt. The SCA,
443 number of averaged pixels in retrieval units, and fitting residual showed an impact on the results of
444 AOD. A larger number of pixels in retrieval units and a smaller fitting residual can help improve the
445 quality of retrieval. By quality control (removing pixels: SCA > 150; number of averaged pixels <
446 4; length of timesteps < 5; non-polarized fitting residual > 8%; polarized fitting residual > 0.06), the
447 R and EE% of DPC GRASP/Models AOD improve to 0.9007 and 82.54%, respectively. The
448 corresponding MB and RMSE decreased from 0.0256 and 0.0842 to 0.0234 and 0.0662, respectively.
449 This indicated that DPC has a good ability to detect aerosols under this scheme.

450 In the perspective of spatial scale, the R and EE% of GRASP/Models were larger than 0.9 and
451 80% respectively at ~~the~~ most AERONET sites. Large RMSE and Low EE% were found in heavy
452 aerosol loading conditions such as Asia and Africa. When the actual AOD ~~is~~ was large, the retrieval
453 bias of AOD from satellite observations ~~will~~ would be amplified as reflected in RMSE and EE% to
454 some extent. By compared with MODIS aerosol products, the AOD from DPC GRASP/Models
455 showed good consistency in China, with all heavy aerosol loading regions were detected. However,
456 the values of AOD ~~are~~ were underestimated by DPC, probably due to overstrict cloud masking.
457 Evaluation of the time-serial AOD showed the performance of DPC GRASP/Models ~~is~~ was similar
458 to the MODIS DT and better than MODIS DB and MAIAC products. Therefore, to summarize, the

459 DPC ~~can~~could capture spatial and temporal variations in aerosols. The study improves to our
460 understanding of DPC and ~~finds~~s a solution for retrieving AOD based on GRASP algorithm. The
461 continuous development of multi-angle sensors polarized ~~plays~~plays an important role in aerosol
462 monitoring in the future.

463 **Acknowledgement**

464 This study was funded by the National Key R&D Program of China (Grant No. 2018YFB0504500),
465 National Natural Science Foundation of China (Grant No. 41875038, No. 42071348, and No.
466 42001291), the Key R&D projects in Hubei Province (Grant No. 2021BCA220) and supported by
467 the LIESMARS Special Research Funding. We are grateful to the Moderate Resolution Imaging
468 Spectroradiometer (MODIS) Team, the Aerosol Robotic Network (AERONET) Organization and
469 the GaoFen-5 Directional Polarimetric Camera (DPC) Developed Team for freely distributing their
470 aerosol products and measurements. The numerical calculations in this paper have been done on the
471 supercomputing system in the Supercomputing Center of Wuhan University. Finally, we would also
472 like to thank all reviewers for their constructive and valuable comments.

473 **References**

- 474 Albrecht, B.A. (1989). AEROSOLS, CLOUD MICROPHYSICS, AND FRACTIONAL CLOUDINESS.
475 *Science*, 245, 1227-1230, doi:10.1126/science.245.4923.1227
- 476 Ångström, A. (1964). The Parameter of Atmospheric Turbidity. *Tellus*, 16, 64-75,
477 doi:10.3402/tellusa.v16i1.8885
- 478 Breon, F.M., & Colzy, S. (1999). Cloud detection from the spaceborne POLDER instrument and
479 validation against surface synoptic observations. *Journal of Applied Meteorology*, 38, 777-785,
480 doi:10.1175/1520-0450(1999)038<0777:cdftsp>2.0.co;2
- 481 Breon, F.M., & Goloub, P. (1998). Cloud droplet effective radius from spaceborne polarization
482 measurements. *Geophysical Research Letters*, 25, 1879-1882, doi:10.1029/98gl01221
- 483 Che, H., Yang, L., Liu, C., Xia, X., Wang, Y., Wang, H., Wang, H., Lu, X., & Zhang, X. (2019). Long-
484 term validation of MODIS C6 and C6.1 Dark Target aerosol products over China using CARSNET and
485 AERONET. *Chemosphere*, 236, 124268, doi:10.1016/j.chemosphere.2019.06.238
- 486 Chen, C., Dubovik, O., Fuertes, D., Litvinov, P., Lapyonok, T., Lopatin, A., Ducos, F., Derimian, Y.,
487 Herman, M., Tanré, D., Remer, L.A., Lyapustin, A., Sayer, A.M., Levy, R.C., Hsu, N.C., Descloitres, J.,
488 Li, L., Torres, B., Karol, Y., Herrera, M., Herreras, M., Aspetsberger, M., Wanzenboeck, M., Bindreiter,
489 L., Marth, D., Hangler, A., & Federspiel, C. (2020). Validation of GRASP algorithm product from
490 POLDER/PARASOL data and assessment of multi-angular polarimetry potential for aerosol monitoring.
491 *Earth System Science Data*, 12, 3573-3620, doi:10.5194/essd-12-3573-2020
- 492 Cox, C., & Munk, W. (1954). Measurement Of The Roughness Of The Sea Surface From Photographs
493 Of The Suns Glitter. *Journal Of The Optical Society Of America*, 44, 838-850,
494 doi:10.1364/JOSA.44.000838
- 495 Deschamps, P., Breon, F., Leroy, M., Podaire, A., Bricaud, A., Buriez, J., & Seze, G. (1994). The
496 POLDER mission: instrument characteristics and scientific objectives. *Ieee Transactions on Geoscience
497 and Remote Sensing*, 32, 598-615, doi:10.1109/36.297978

498 Deuzé, J.L., Bréon, F.M., Devaux, C., Goloub, P., Herman, M., Lafrance, B., Maignan, F., Marchand, A.,
499 Nadal, F., Perry, G., & Tanré, D. (2001). Remote sensing of aerosols over land surfaces from POLDER-
500 ADEOS-1 polarized measurements. *Journal of Geophysical Research: Atmospheres*, *106*, 4913-4926,
501 doi:10.1029/2000jd900364

502 Diner, D.J., Beckert, J.C., Reilly, T.H., Bruegge, C.J., Conel, J.E., Kahn, R.A., Martonchik, J.V.,
503 Ackerman, T.P., Davies, R., Gerstl, S.A.W., Gordon, H.R., Muller, J.P., Myneni, R.B., Sellers, P.J., Pinty,
504 B., & Verstraete, M.M. (1998). Multi-angle Imaging SpectroRadiometer (MISR) - Instrument description
505 and experiment overview. *Ieee Transactions on Geoscience and Remote Sensing*, *36*, 1072-1087,
506 doi:10.1109/36.700992

507 Dubovik, O., Fuertes, D., Litvinov, P., Lopatin, A., Lapyonok, T., Dubovik, I., Xu, F., Ducos, F., Chen,
508 C., Torres, B., Derimian, Y., Li, L., Herreras-Giralda, M., Herrera, M., Karol, Y., Matar, C., Schuster,
509 G.L., Espinosa, R., Puthukkudy, A., Li, Z., Fischer, J., Preusker, R., Cuesta, J., Kreuter, A., Cede, A.,
510 Aspetsberger, M., Marth, D., Bindreiter, L., Hangler, A., Lanzinger, V., Holter, C., & Federspiel, C.
511 (2021). A Comprehensive Description of Multi-Term LSM for Applying Multiple a Priori Constraints in
512 Problems of Atmospheric Remote Sensing: GRASP Algorithm, Concept, and Applications. *Frontiers in*
513 *Remote Sensing*, *2:706851*, doi:10.3389/frsen.2021.706851

514 Dubovik, O., Herman, M., Holdak, A., Lapyonok, T., Tanre, D., Deuze, J.L., Ducos, F., Sinyuk, A., &
515 Lopatin, A. (2011). Statistically optimized inversion algorithm for enhanced retrieval of aerosol
516 properties from spectral multi-angle polarimetric satellite observations. *Atmospheric Measurement*
517 *Techniques*, *4*, 975-1018, doi:10.5194/amt-4-975-2011

518 Dubovik, O., & King, M.D. (2000). A flexible inversion algorithm for retrieval of aerosol optical
519 properties from Sun and sky radiance measurements. *Journal of Geophysical Research Atmospheres*, *105*,
520 20673-20696, doi:10.1029/2000JD900282

521 Dubovik, O., Lapyonok, T., Litvinov, P., Herman, M., Fuertes, D., Ducos, F., Lopatin, A., Chaikovsky,
522 A., Torres, B., Derimian, Y., Huang, X., Aspetsberger, M., & Federspiel, C. (2014). GRASP: a versatile
523 algorithm for characterizing the atmosphere. *SPIE Newsroom*, doi:10.1117/2.1201408.005558

524 Dubovik, O., Li, Z., Mishchenko, M.I., Tanré, D., Karol, Y., Bojkov, B., Cairns, B., Diner, D.J., Espinosa,
525 W.R., Goloub, P., Gu, X., Hasekamp, O., Hong, J., Hou, W., Knobelspiesse, K.D., Landgraf, J., Li, L.,
526 Litvinov, P., Liu, Y., Lopatin, A., Marbach, T., Maring, H., Martins, V., Meijer, Y., Milinevsky, G., Mukai,
527 S., Parol, F., Qiao, Y., Remer, L., Rietjens, J., Sano, I., Stammes, P., Stammes, S., Sun, X., Tabary, P.,
528 Travis, L.D., Waquet, F., Xu, F., Yan, C., & Yin, D. (2019). Polarimetric remote sensing of atmospheric
529 aerosols: Instruments, methodologies, results, and perspectives. *Journal of Quantitative Spectroscopy*
530 *and Radiative Transfer*, *224*, 474-511, doi:10.1016/j.jqsrt.2018.11.024

531 Dubovik, O., Sinyuk, A., Lapyonok, T., Holben, B.N., Mishchenko, M., Yang, P., Eck, T.F., Volten, H.,
532 Munoz, O., Veihelmann, B., van der Zande, W.J., Leon, J.F., Sorokin, M., & Slutsker, I. (2006).
533 Application of spheroid models to account for aerosol particle nonsphericity in remote sensing of desert
534 dust. *Journal of Geophysical Research-Atmospheres*, *111*, D11208, doi:10.1029/2005jd006619

535 Eck, T.F., Holben, B.N., Reid, J.S., Dubovik, O., Smirnov, A., O'Neill, N.T., Slutsker, I., & Kinne, S.
536 (1999). Wavelength dependence of the optical depth of biomass burning, urban, and desert dust aerosols.
537 *Journal of Geophysical Research: Atmospheres*, *104*, 31333-31349, doi:10.1029/1999jd900923

538 Eck, T.F., Holben, B.N., Sinyuk, A., Pinker, R.T., Goloub, P., Chen, H., Chatenet, B., Li, Z., Singh, R.P.,
539 Tripathi, S.N., Reid, J.S., Giles, D.M., Dubovik, O., O'Neill, N.T., Smirnov, A., Wang, P., & Xia, X.
540 (2010). Climatological aspects of the optical properties of fine/coarse mode aerosol mixtures. *Journal of*
541 *Geophysical Research*, *115*, D19205, doi:10.1029/2010jd014002

542 Gao, J., Woodward, A., Vardoulakis, S., Kovats, S., Wilkinson, P., Li, L., Xu, L., Li, J., Yang, J., Li, J.,
543 Cao, L., Liu, X., Wu, H., & Liu, Q. (2017). Haze, public health and mitigation measures in China: A
544 review of the current evidence for further policy response. *Science of the Total Environment*, *578*, 148-
545 157, doi:<https://doi.org/10.1016/j.scitotenv.2016.10.231>

546 Ge, B., Mei, X., Li, Z., Hou, W., Xie, Y., Zhang, Y., Xu, H., Li, K., & Wei, Y. (2020). An improved
547 algorithm for retrieving high resolution fine-mode aerosol based on polarized satellite data: Application
548 and validation for POLDER-3. *Remote Sensing of Environment*, *247*, 111894,
549 doi:10.1016/j.rse.2020.111894

550 Goloub, P., & Deuze, J.L. (1994). Analysis of the POLDER polarization measurements performed over
551 cloud covers. *IEEE Transactions on Geoscience & Remote Sensing*, *32*, 78-88, doi:10.1109/36.285191

552 Gomez-Chova, L., Camps-Valls, G., Calpe-Maravilla, J., Guanter, L., & Moreno, J. (2007). Cloud-
553 screening algorithm for ENVISAT/MERIS multispectral images. *Ieee Transactions on Geoscience and*
554 *Remote Sensing*, *45*, 4105-4118, doi:10.1109/tgrs.2007.905312

555 Guo, J., Deng, M., Lee, S.S., Wang, F., Li, Z., Zhai, P., Liu, H., Lv, W., Yao, W., & Li, X. (2016). Delaying
556 precipitation and lightning by air pollution over the Pearl River Delta. Part I: Observational analyses.
557 *Journal of Geophysical Research: Atmospheres*, *121*, 6472-6488, doi:10.1002/2015jd023257

558 Gupta, P., Remer, L.A., Levy, R.C., & Mattoo, S. (2018). Validation of MODIS 3 km land aerosol optical
559 depth from NASA's EOS Terra and Aqua missions. *Atmospheric Measurement Techniques*, *11*, 3145-
560 3159, doi:10.5194/amt-11-3145-2018

561 Hagolle, O., Goloub, P., Deschamps, P.-Y., Cosnefroy, H., Briottet, X., Bailleul, T., Nicolas, J.-M., Parol,
562 F., Lafrance, B., & Herman, M. (1999). Results of POLDER in-flight calibration. *Ieee Transactions on*
563 *Geoscience and Remote Sensing*, *37*, 1550-1566, doi:10.1109/36.763266

564 Holben, B.N., Eck, T.F., Slutsker, I., Tanre, D., Buis, J.P., Setzer, A., Vermote, E., Reagan, J.A., Kaufman,
565 Y.J., Nakajima, T., Lavenu, F., Jankowiak, I., & Smirnov, A. (1998). AERONET - A federated instrument
566 network and data archive for aerosol characterization. *Remote Sensing of Environment*, *66*, 1-16,
567 doi:10.1016/s0034-4257(98)00031-5

568 Hsu, N.C., Jeong, M.J., Bettenhausen, C., Sayer, A.M., Hansell, R., Seftor, C.S., Huang, J., & Tsay, S.C.
569 (2013). Enhanced Deep Blue aerosol retrieval algorithm: The second generation. *Journal of Geophysical*
570 *Research: Atmospheres*, *118*, 9296-9315, doi:10.1002/jgrd.50712

571 Hsu, N.C., Tsay, S.C., King, M.D., & Herman, J.R. (2004). Aerosol properties over bright-reflecting
572 source regions. *IEEE Transactions on Geoscience & Remote Sensing*, *42*, 557-569,
573 doi:10.1109/TGRS.2004.824067

574 Jin, S., Ma, Y., Zhang, M., Gong, W., Dubovik, O., Liu, B., Shi, Y., & Yang, C. (2019). Retrieval of 500
575 m Aerosol Optical Depths from MODIS Measurements over Urban Surfaces under Heavy Aerosol
576 Loading Conditions in Winter. *Remote Sensing*, *11*, 2218, doi:10.3390/rs11192218

577 Jin, S., Zhang, M., Ma, Y., Gong, W., Chen, C., Yang, L., Hu, X., Liu, B., Chen, N., Du, B., & Shi, Y.
578 (2021). Adapting the Dark Target Algorithm to Advanced MERSI Sensor on the FengYun-3-D Satellite:
579 Retrieval and Validation of Aerosol Optical Depth Over Land. *Ieee Transactions on Geoscience and*
580 *Remote Sensing*, *59*, 8781-8797, doi:10.1109/TGRS.2020.3021021

581 Kacenenbogen, M., Leon, J.F., Chiapello, I., & Tanre, D. (2006). Characterization of aerosol pollution
582 events in France using ground-based and POLDER-2 satellite data. *Atmospheric Chemistry and Physics*,
583 *6*, 4843-4849, doi:10.5194/acp-6-4843-2006

584 Kaufman, Y.J., Tanré, D., Gordon, H.R., Nakajima, T., Lenoble, J., Frouin, R., Grassl, H., Herman, B.M.,
585 King, M.D., & Teillet, P.M. (1997). Passive remote sensing of tropospheric aerosol and atmospheric

586 correction for the aerosol effect. *Journal of Geophysical Research: Atmospheres*, 102, 16815-16830,
587 doi:10.1029/97jd01496

588 Koren, I., Remer, L.A., Kaufman, Y.J., Rudich, Y., & Martins, J.V. (2007). On the twilight zone between
589 clouds and aerosols. *Geophysical Research Letters*, 34, L08805, doi:10.1029/2007gl029253

590 Lenoble, J., Remer, L., & Tanre, D. (2013). *Aerosol Remote Sensing*. Springer-Verlag Berlin Heidelberg,
591 doi:10.1007/978-3-642-17725-5

592 Levy, R.C., Mattoo, S., Munchak, L.A., Remer, L.A., Sayer, A.M., Patadia, F., & Hsu, N.C. (2013). The
593 Collection 6 MODIS aerosol products over land and ocean. *Atmospheric Measurement Techniques*, 6,
594 2989-3034, doi:10.5194/amt-6-2989-2013

595 Li, J.H., Ma, J.J., Li, C., Wang, Y.Y., Li, Z.Q., & Hong, J. (2021). Multi-information collaborative cloud
596 identification algorithm in Gaofen-5 Directional Polarimetric Camera imagery. *Journal of Quantitative
597 Spectroscopy & Radiative Transfer*, 261, 107439, doi:10.1016/j.jqsrt.2020.107439

598 Li, L., Che, H., Zhang, X., Chen, C., Chen, X., Gui, K., Liang, Y., Wang, F., Derimian, Y., Fuertes, D.,
599 Dubovik, O., Zheng, Y., Zhang, L., Guo, B., Wang, Y., & Zhang, X. (2022). A satellite-measured view of
600 aerosol component content and optical property in a haze-polluted case over North China Plain.
601 *Atmospheric Research*, 266, 105958, doi:<https://doi.org/10.1016/j.atmosres.2021.105958>

602 Li, L., Dubovik, O., Derimian, Y., Schuster, G.L., Lapyonok, T., Litvinov, P., Ducos, F., Fuertes, D., Chen,
603 C., Li, Z., Lopatin, A., Torres, B., & Che, H. (2019). Retrieval of aerosol components directly from
604 satellite and ground-based measurements. *Atmospheric Chemistry and Physics*, 19, 13409-13443,
605 doi:10.5194/acp-19-13409-2019

606 Li, X., & Strahler, A.H. (1992). Geometric-optical bidirectional reflectance modeling of the discrete
607 crown vegetation canopy: effect of crown shape and mutual shadowing. *Ieee Transactions on Geoscience
608 and Remote Sensing*, 30, 276-292, doi:10.1109/36.134078

609 Li, Z., Hou, W., Hong, J., Zheng, F., Luo, D., Wang, J., Gu, X., & Qiao, Y. (2018). Directional
610 Polarimetric Camera (DPC): Monitoring aerosol spectral optical properties over land from satellite
611 observation. *Journal of Quantitative Spectroscopy and Radiative Transfer*, 218, 21-37,
612 doi:10.1016/j.jqsrt.2018.07.003

613 Li, Z.Q., Lau, W.K.M., Ramanathan, V., Wu, G., Ding, Y., Manoj, M.G., Liu, J., Qian, Y., Li, J., Zhou,
614 T., Fan, J., Rosenfeld, D., Ming, Y., Wang, Y., Huang, J., Wang, B., Xu, X., Lee, S.S., Cribb, M., Zhang,
615 F., Yang, X., Zhao, C., Takemura, T., Wang, K., Xia, X., Yin, Y., Zhang, H., Guo, J., Zhai, P.M., Sugimoto,
616 N., Babu, S.S., & Brasseur, G.P. (2016). Aerosol and monsoon climate interactions over Asia. *Reviews
617 of Geophysics*, 54, 866-929, doi:10.1002/2015rg000500

618 Liu, B., Ma, X., Ma, Y., Li, H., Jin, S., Fan, R., & Gong, W. (2022). The relationship between atmospheric
619 boundary layer and temperature inversion layer and their aerosol capture capabilities. *Atmospheric
620 Research*, 271, 106121, doi:10.1016/j.atmosres.2022.106121

621 Lopatin, A., Dubovik, O., Fuertes, D., Stenchikov, G., Lapyonok, T., Veselovskii, I., Wienhold, F.G.,
622 Shevchenko, I., Hu, Q., & Parajuli, S. (2021). Synergy processing of diverse ground-based remote
623 sensing and in situ data using the GRASP algorithm: applications to radiometer, lidar and radiosonde
624 observations. *Atmos. Meas. Tech.*, 14, 2575-2614, doi:10.5194/amt-14-2575-2021

625 Lyapustin, A., Wang, Y., Korkin, S., & Dong, H. (2018). MODIS Collection 6 MAIAC algorithm.
626 *Atmospheric Measurement Techniques*, 11, 5741-5765, doi:10.5194/amt-11-5741-2018

627 Ma, Y., Zhu, Y., Liu, B., Li, H., Jin, S., Zhang, Y., Fan, R., & Gong, W. (2021). Estimation of the vertical
628 distribution of particle matter (PM_{2.5}) concentration and its transport flux from lidar measurements
629 based on machine learning algorithms. *Atmospheric Chemistry and Physics*, 21, 17003-17016,

630 doi:10.5194/acp-21-17003-2021

631 Martins, J.V., Tanré, D., Remer, L., Kaufman, Y., Mattoo, S., & Levy, R. (2002). MODIS Cloud screening
632 for remote sensing of aerosols over oceans using spatial variability. *Geophysical Research Letters*, *29*,
633 MOD4, doi:10.1029/2001GL013252

634 McCormick, M.P., Hamill, P., Pepin, T.J., Chu, W.P., Swissler, T.J., & McMaster, L.R. (1979).
635 SATELLITE STUDIES OF THE STRATOSPHERIC AEROSOL. *Bulletin of the American*
636 *Meteorological Society*, *60*, 1038-1046, doi:10.1175/1520-0477(1979)060<1038:ssotsa>2.0.co;2

637 Mishchenko, M.I., & Travis, L.D. (1997). Satellite retrieval of aerosol properties over the ocean using
638 polarization as well as intensity of reflected sunlight. *Journal of Geophysical Research: Atmospheres*,
639 *102*, 16989-17013, doi:<https://doi.org/10.1029/96JD02425>

640 Nadal, F., & Bréon, F.M. (1999). Parameterization of Surface Polarized Reflectance Derived from
641 POLDER Spaceborne Measurements. *IEEE Transactions on Geoscience & Remote Sensing*, *37*, 1709-
642 1718, doi:10.1109/36.763292

643 Nakajima, T., Yoon, S.C., Ramanathan, V., Shi, G.Y., Takemura, T., Higurashi, A., Takamura, T., Aoki,
644 K., Sohn, B.J., Kim, S.W., Tsuruta, H., Sugimoto, N., Shimizu, A., Tanimoto, H., Sawa, Y., Lin, N.H.,
645 Lee, C.T., Goto, D., & Schutgens, N. (2007). Overview of the Atmospheric Brown Cloud East Asian
646 Regional Experiment 2005 and a study of the aerosol direct radiative forcing in east Asia. *Journal of*
647 *Geophysical Research-Atmospheres*, *112*, 23, doi:10.1029/2007jd009009

648 Ou, Y., Li, L., Ying, Z., Dubovik, O., Derimian, Y., Chen, C., Fuertes, D., Xie, Y., Lopatin, A., Ducos, F.,
649 & Peng, Z. (2021). Spatio-Temporal Variability of Aerosol Components, Their Optical and
650 Microphysical Properties over North China during Winter Haze in 2012, as Derived from
651 POLDER/PARASOL Satellite Observations. *Remote Sensing*, *13*, 2682, doi:10.3390/rs13142682

652 Qie, L., Li, Z., Zhu, S., Xu, H., Xie, Y., Qiao, R., Hong, J., & Tu, B. (2021). In-flight radiometric and
653 polarimetric calibration of the Directional Polarimetric Camera onboard the GaoFen-5 satellite over the
654 ocean. *Appl Opt*, *60*, 7186-7199, doi:10.1364/AO.422980

655 Rao, C.R.N., Stowe, L.L., & McClain, E.P. (1989). REMOTE-SENSING OF AEROSOLS OVER THE
656 OCEANS USING AVHRR DATA THEORY, PRACTICE AND APPLICATIONS. *International Journal*
657 *of Remote Sensing*, *10*, 743-749, doi:10.1080/01431168908903915

658 Remer, L.A., Mattoo, S., Levy, R.C., Heidinger, A., Pierce, R.B., & Chin, M. (2012). Retrieving aerosol
659 in a cloudy environment: aerosol product availability as a function of spatial resolution. *Atmospheric*
660 *Measurement Techniques*, *5*, 1823-1840, doi:10.5194/amt-5-1823-2012

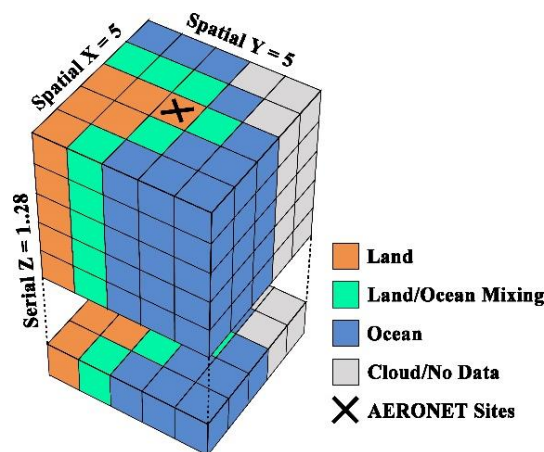
661 Rosenfeld, D., Lohmann, U., Raga, G.B., O'Dowd, C.D., Kulmala, M., Fuzzi, S., Reissell, A., & Andreae,
662 M.O. (2008). Flood or drought: How do aerosols affect precipitation? *Science*, *321*, 1309-1313,
663 doi:10.1126/science.1160606

664 Sayer, A.M., Hsu, N.C., Bettenhausen, C., & Jeong, M.J. (2013). Validation and uncertainty estimates
665 for MODIS Collection 6 "Deep Blue" aerosol data. *Journal of Geophysical Research: Atmospheres*, *118*,
666 7864-7872, doi:10.1002/jgrd.50600

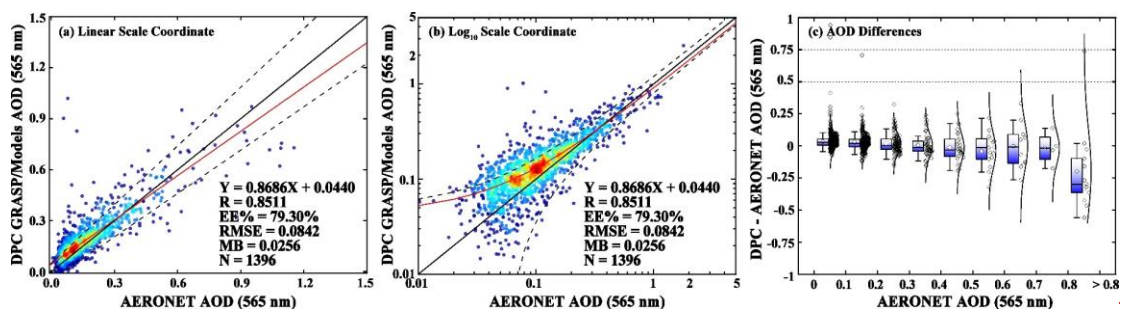
667 Sayer, A.M., Munchak, L.A., Hsu, N.C., Levy, R.C., Bettenhausen, C., & Jeong, M.J. (2014). MODIS
668 Collection 6 aerosol products: Comparison between Aqua's e-Deep Blue, Dark Target, and "merged" data
669 sets, and usage recommendations. *Journal of Geophysical Research-Atmospheres*, *119*, 13965-13989,
670 doi:10.1002/2014jd022453

671 Shi, T., Han, G., Ma, X., Gong, W., Chen, W., Liu, J., Zhang, X., Pei, Z., Gou, H., & Bu, L. (2021).
672 Quantifying CO₂ Uptakes Over Oceans Using LIDAR: A Tentative Experiment in Bohai Bay.
673 *Geophysical Research Letters*, *48*, e2020GL091160, doi:<https://doi.org/10.1029/2020GL091160>

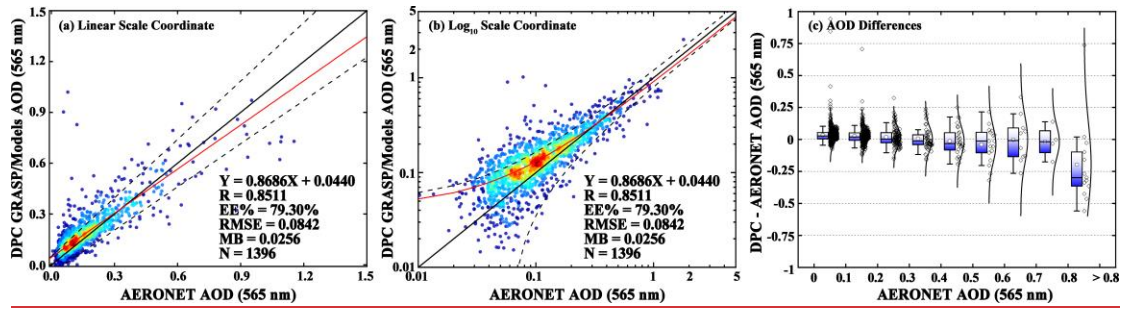
674 Tanre, D., Breon, F.M., Deuze, J.L., Dubovik, O., Ducos, F., Francois, P., Goloub, P., Herman, M.,
 675 Lifermann, A., & Waquet, F. (2011). Remote sensing of aerosols by using polarized, directional and
 676 spectral measurements within the A-Train: the PARASOL mission. *Atmospheric Measurement*
 677 *Techniques*, 4, 1383-1395, doi:10.5194/amt-4-1383-2011
 678 Tegen, I., & Lacis, A.A. (1996). Modeling of particle size distribution and its influence on the radiative
 679 properties of mineral dust aerosol. *Journal of Geophysical Research Atmospheres*, 101, 19237-19244,
 680 doi:10.1029/95JD03610
 681 Zhang, M., Jin, S., Ma, Y., Fan, R., Wang, L., Gong, W., & Liu, B. (2021). Haze events at different levels
 682 in winters: A comprehensive study of meteorological factors, Aerosol characteristics and direct radiative
 683 forcing in megacities of north and central China. *Atmospheric Environment*, 245, 118056,
 684 doi:<https://doi.org/10.1016/j.atmosenv.2020.118056>
 685 Zhdanova, E.Y., Chubarova, N.Y., & Lyapustin, A.I. (2020). Assessment of urban aerosol pollution over
 686 the Moscow megacity by the MAIAC aerosol product. *Atmospheric Measurement Techniques*, 13, 877-
 687 891, doi:10.5194/amt-13-877-2020
 688 Zhu, S., Li, Z., Qie, L., Xu, H., Ge, B., Xie, Y., Qiao, R., Xie, Y., Hong, J., Meng, B., Tu, B., & Chen, F.
 689 (2022). In-Flight Relative Radiometric Calibration of a Wide Field of View Directional Polarimetric
 690 Camera Based on the Rayleigh Scattering over Ocean. *Remote Sensing*, 14, doi:10.3390/rs14051211
 691 Zhu, Z., & Woodcock, C.E. (2012). Object-based cloud and cloud shadow detection in Landsat imagery.
 692 *Remote Sensing of Environment*, 118, 83-94, doi:10.1016/j.rse.2011.10.028
 693



694
 695 **Figure 1.** Schematic diagram for multi-pixel retrieval unit ($5 \times 5 \times 1..28$). A maximum of 28 sequences
 696 allowed in each unit is limited by hardware memory.
 697



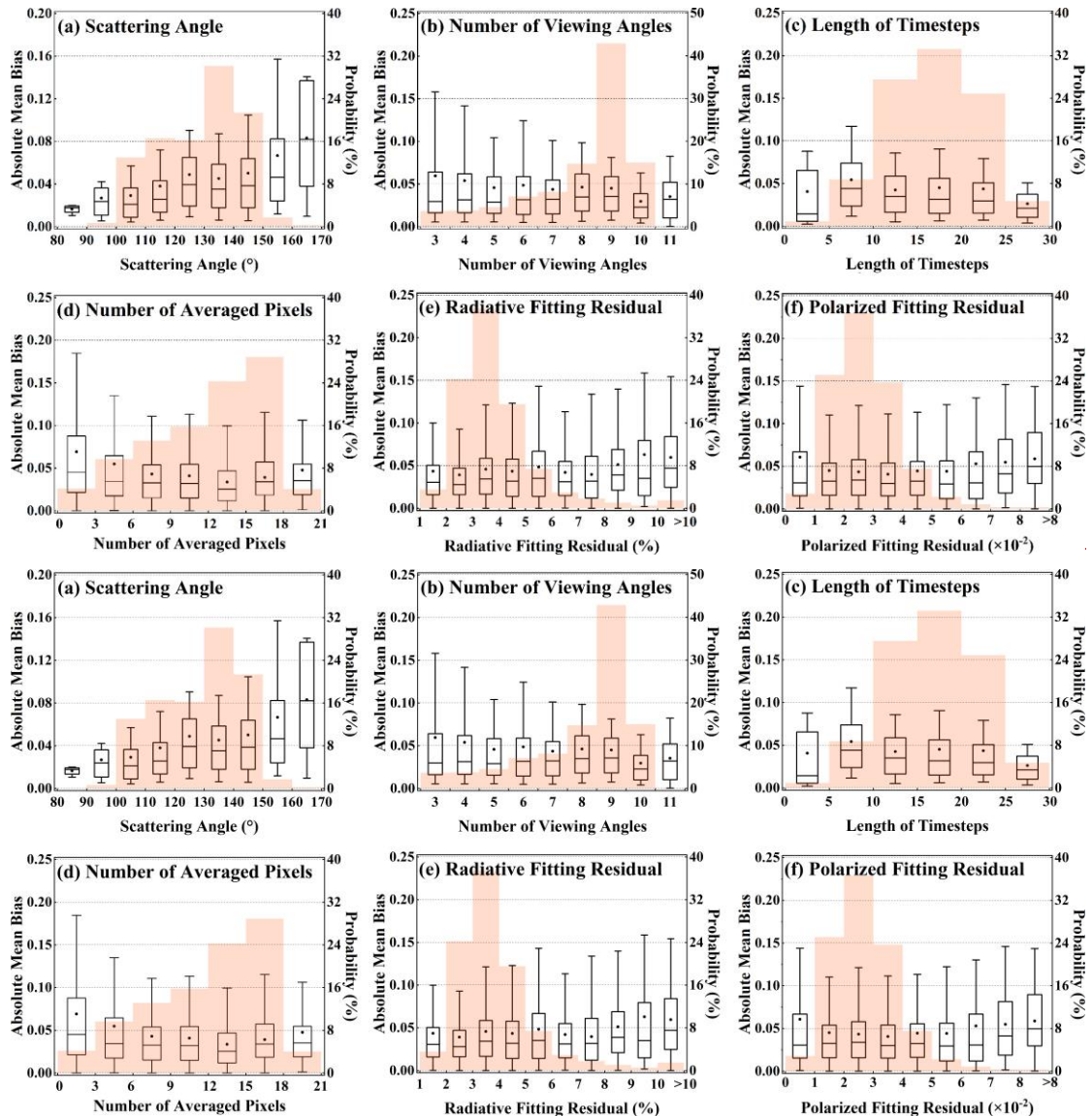
698



699

700 **Figure 2.** (a) Density scatterplot of AOD retrievals from DPC with the GRASP/Models scheme
 701 versus the AERONET observations with a linear coordinate system. (b) The density scatterplot with
 702 a logarithmic coordinate system. The solid black line is the one to one and the dashed black lines
 703 show the ranges of Expected Error. The red solid lines represent the linear regression line; (c) Box
 704 plots show changes of differences between DPC GRASP/Models and AEROENT with AOD
 705 increasing. Diamond marks and curves represent distributions of sample and normal distribution
 706 fitting lines, respectively.

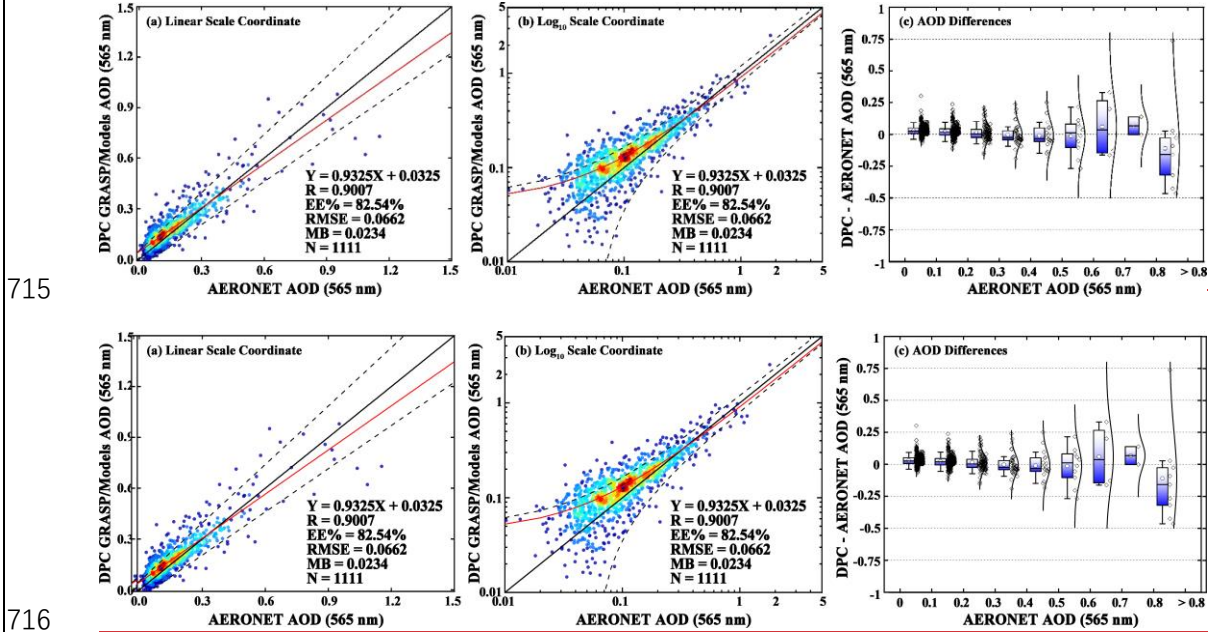
707



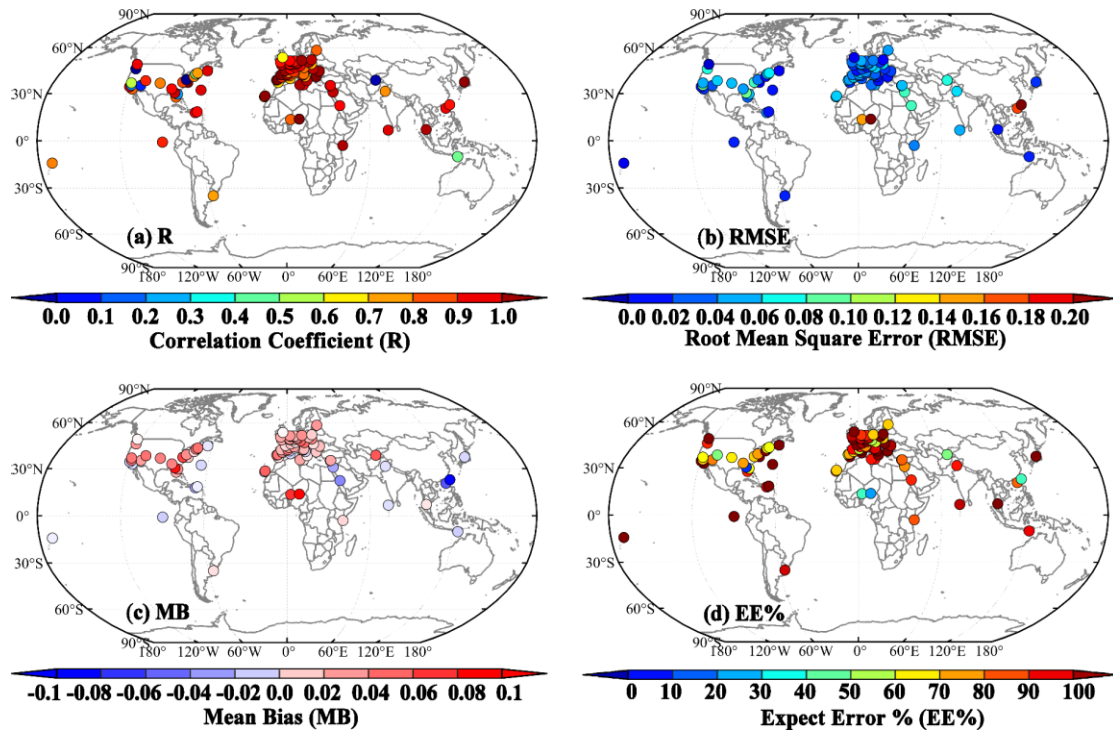
708

709

710 **Figure 3.** Influencing factors of AOD retrieval performance of DPC based on the GRASP/Models:
 711 **(a)** SCA; **(b)** number of viewing angles; **(c)** length of timesteps; **(d)** number of averaged pixels; **(e)**
 712 non-polarized fitting residual; **(f)** polarized fitting residual. Orange shadows in the background
 713 represents the probability distribution of the samples.
 714

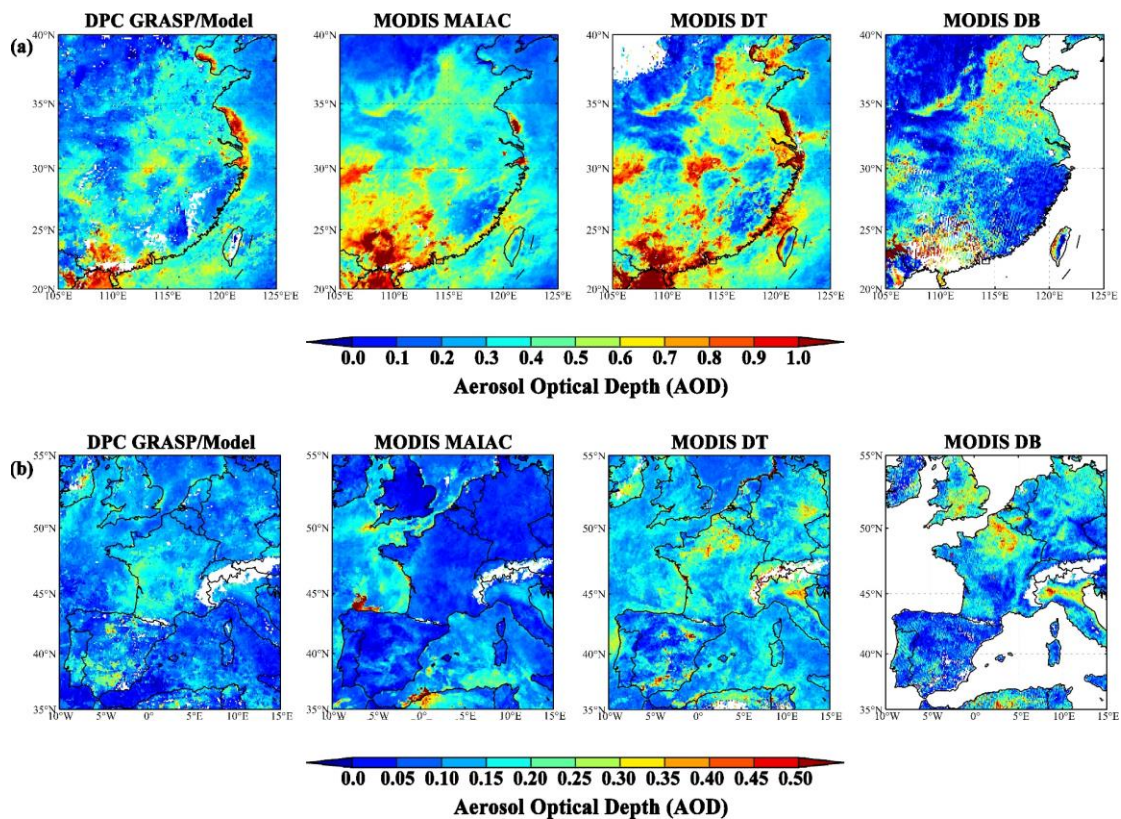


717 **Figure 4.** **(a)** Density scatterplot of AOD retrievals from DPC with the GRASP/Models scheme
 718 versus the AERONET observations with a logarithmic coordinate system after quality control. **(b)**
 719 The density scatterplot with a logarithmic coordinate system. The solid black lines are diagonal and
 720 the dashed black lines show the ranges of Expected Error. The red solid lines represent the linear
 721 regression line; **(c)** Box plots show changes of differences between DPC GRASP/Models and
 722 AEROENT with AOD increasing. Diamond marks and curves represent distributions of sample and
 723 normal distribution fitting lines, respectively.
 724
 725



726
727
728
729
730

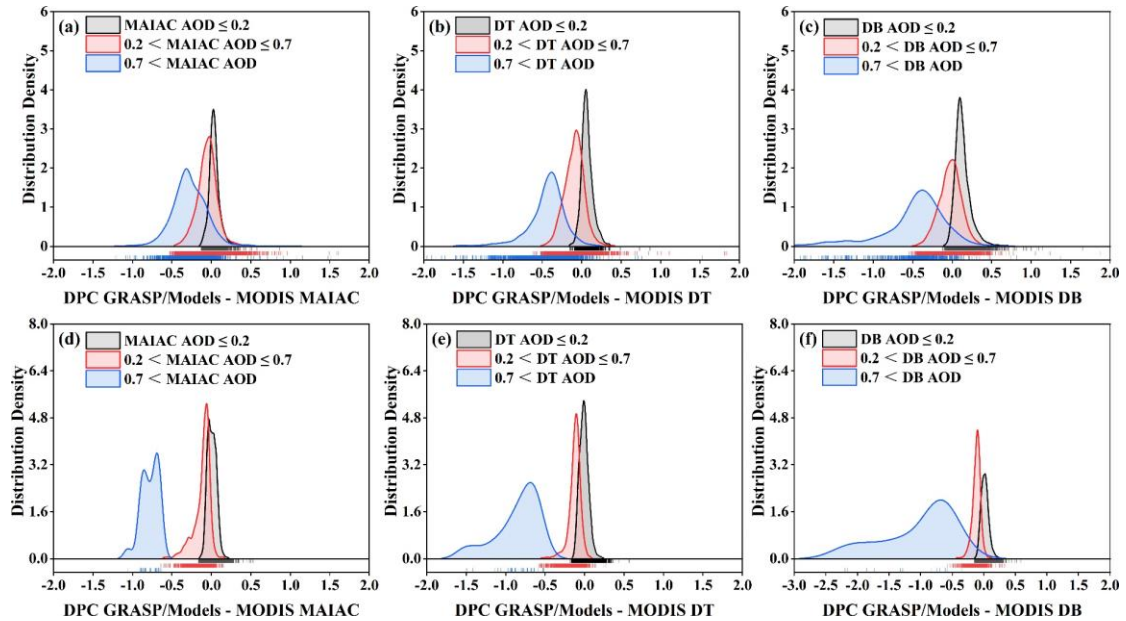
Figure 5. Spatial Distributions of (a) R, (b) RMSE, (c) MB, and (d) EE% calculated from DPC GRASP/Models by compared with AERONET observations. Only sites with more than 5 matching points are included.



731
732
733

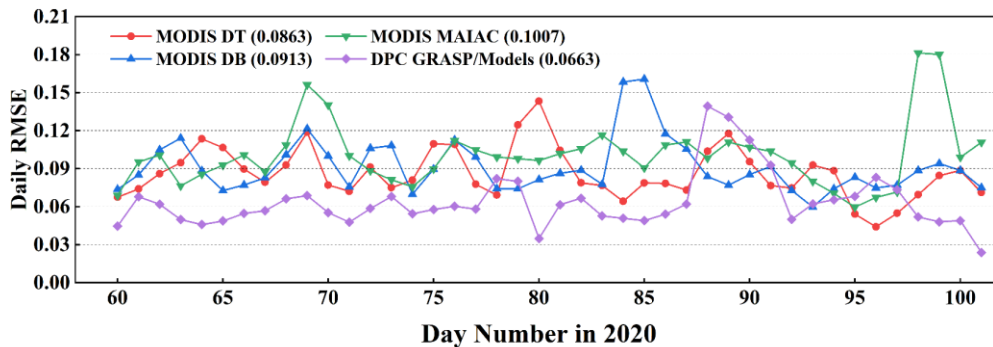
Figure 6. Spatial distribution of AOD from DPC GRASP/Models compared with MODIS MAIMC, DT, and DB aerosol products in March, 2020: (a) Eastern and Southern China with its adjacent sea

734 areas; (b) Areas of Western Europe including the Atlantic Ocean and the Mediterranean. The DPC
 735 AOD is at 565 nm and the MODIS AOD is at 550 nm.
 736



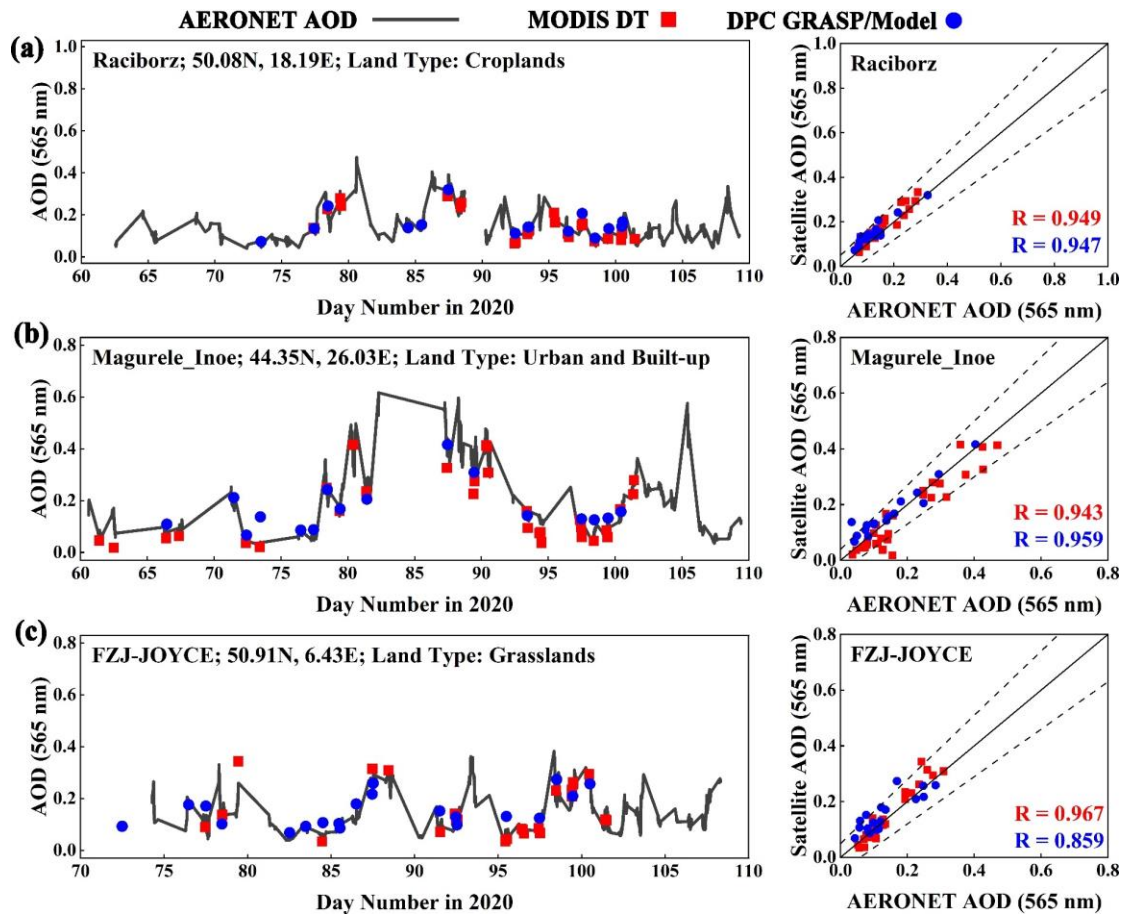
737
 738 **Figure 7.** Distribution Density of AOD differences between DPC GRASP/Models and MODIS DT,
 739 DB, and MAIAC products at: (a-c) Eastern and Southern China with its adjacent sea areas; (d-e)
 740 Areas of Western Europe including the Atlantic Ocean and the Mediterranean. It is noted that the
 741 MODIS DB product only releases terrestrial AOD data.

742
 743



744
 745 **Figure 8.** Time series of daily RMSE for the selected AERONET stations during March and April
 746 of 2020. The number in brackets are averaged values of daily RMSE. The positions of AERONET
 747 stations are the same with **Figure 5**.

748



749
750
751
752
753

Figure 9. Time series of AOD from the DPC GRASP/Models versus the MODIS DT products and AERONET observations at three sites as cases: **(a)** Raciborz, **(b)** Magurele_Inoe, and **(c)** FZJ-JOYCE. The scatterplot shows the relationship between AERONET AOD and satellite AOD.